Chemical-shift gamma-encoding nuclear magnetic resonance for uniaxially oriented matter under sample spinning

Nishiyama, Y; Kubo, A; Terao, T

Chemical-shift γ-encoding nuclear magnetic resonance for uniaxially oriented matter under sample spinning

Yusuke Nishiyama,[a] Atsushi Kubo, and Takehiko Terao[b]
Department of Chemistry, Graduate School of Science, Kyoto University, Kyoto, 606-8502 Japan

(Received 11 February 2002; accepted 9 May 2003)

Two approaches are proposed by which chemical shift anisotropies (CSAs) in uniaxially oriented matter can be obtained from the positions of sharp peaks under sample spinning. Both rely on the removal of broadening due to the γ dependence of the resonance frequency, where γ is the third angle of the Euler angles describing the orientation of the chemical shift tensor in the sample symmetry-axis frame. In one approach, an inversion pulse train recovers the γ-dependent CSAs, and the free-induction decay is transformed into sharp lines by γ-encoding transformation. In the other, the free-induction decay signal due to γ-dependent anisotropic chemical shifts is observed by rf-field inhomogeneity-compensated rotary resonance, and the CSAs are represented as the positions of sharp lines by Fourier transformation. The effects of finite pulse width, rf-amplitude missetting, rf-field inhomogeneity, and resonance offset are theoretically and experimentally investigated for both approaches. When the orientation of the sample symmetry axis in the CSA principal axis system distributes around the central orientation to some extent, peaks in γ-encoded two-dimensional (2D) spectra under off-magic-angle spinning show two-dimensionally broadened line shapes. It is theoretically shown that the orientational distribution can be directly obtained by transforming the 2D spectrum on the basis of the one-to-one correspondence between the peak position and the symmetry axis orientation. The ^{13}C CSA in uniaxially drawn polyethylene and the ^{13}C CSA with the orientational distribution in uniaxially drawn polypropylene are obtained from the γ-encoded 2D spectra. © *2003 American Institute of Physics.* [DOI: 10.1063/1.1587701]

I. INTRODUCTION

The chemical shift anisotropy (CSA) of a nuclear spin in a powder sample represents a peculiarly broadened line shape called a powder pattern.[1,2] The three principal values of the CSA tensor are usually obtained by simulating the powder pattern. The principal values provide useful structural information about the nuclear site.

We can conveniently and accurately determine three principal values, if we can observe sharp lines at the positions given by three independent functions of the principal values for each CSA tensor in a powder sample either simultaneously or by different experiments. This was realized by dephasing the signals other than those corresponding to the principal values.[3] However, such an approach causes a loss of sensitivity, because only a subset of the spins in the sample is observed. de Swiet proposed a two-dimensional (2D) transformation which converts a 2D CSA powder pattern into three sharp *anisotropic* peaks[4,5] and performed a 3D experiment to determine the individual sets of the principal values of chemically distinct CSA tensors.[5] Such anisotropic peaks to which all the spins contribute cannot generally be observed by 1D NMR, even if any rf pulses, any rf-field modulation, and any 3D sample rotation with any time-dependent spinning speed are incorporated.[6]

Recently, for uniaxially oriented matter with a unique chemical site, we showed that an analytical transformation of the free induction decay (FID) represents the anisotropic peak, when the sample symmetry axis is aligned perpendicular to the magnetic field direction in static sample conditions.[7] The transformation, which we refer to as the γ-encoding transformation (GET), removes line broadening (γ broadening) due to the distribution of the CSA tensor orientation around the sample symmetry axis. On the other hand, off-magic-angle spinning (OMAS) around the symmetry axis also removes the γ broadening.[1,2,7] GET, OMAS, and magic-angle spinning (MAS) provide different shifts given by independent functions of the principal values. Thus, the three sharp lines separately obtained by 1D NMR allow us to determine the CSA principal values accurately without necessity of simulation when the orientation of the symmetry axis in the principal axis system (PAS) is known or, conversely, the symmetry axis orientation when the principal values are known. However, we cannot apply this method to static samples with multiple chemical sites.

In the present study, we extend the above γ-encoding method so that it can be applied to the case where more than one chemically distinct site exists. In the expanded methods, a uniaxially oriented sample is spun around the symmetry axis at the magic angle or an off-magic angle and an inversion-pulse train is applied synchronously with the sample rotation. Several methods are proposed, which are classified into two approaches. In the first approach, a pulse sequence reintroduces γ broadening, and the resultant FID is

[a]Present address: RIKEN Genomic Sciences Center, Suehiro-cho, Tsurumi, Yokohama, Kanagawa, 230-0045 Japan.
[b]Author to whom correspondence should be addressed. Electronic mail: terao@kuchem.kyoto-u.ac.jp

transformed into sharp anisotropic lines by GET. The second approach relies on a γ-encoded sequence, by which the same anisotropic shift as above except for the scaling factor can be observed using Fourier transform (FT). Several sequences are proposed for the two approaches and discussed from the viewpoint of rf-amplitude missetting, rf-field inhomogeneity, and resonance offset. We also propose the 2D experiment under OMAS conditions in which one of the γ-encoding methods applied in the t_1 period and the OMAS spectrum is observed in the t_2 period. Thus, we can obtain the anisotropic-shift correlation 2D spectrum from which we can determine the anisotropies individually for chemically distinct sites from the positions of the sharp peaks. The present approaches would be useful for studies of uniaxially oriented matter such as drawn fibers or films of polymers,[2] oriented DNA,[8,9] oriented biomembranes,[10] and oriented crystallites of heme proteins.[11] In these samples, the symmetry axis orientation in the PAS generally distributes around the central orientation to some degree, causing broadening in the 2D peaks. The present methods give the orientation distribution from the 2D spectrum, when the principal values are known. The DECODER experiment[12,13] also provides the distribution, which correlates the resonance frequencies at two or three orientations by flipping the sample during the mixing time, when the principal values of the CSA tensor are known. Our approaches do not require such a sample-flipping system.

II. THEORY

We consider a uniaxially oriented sample with an isolated spin 1/2 under sample spinning. We define the rotor-fixed frame with the z^{rot} axis parallel to the spinning axis and the laboratory frame with the z^{lab} axis parallel to the magnetic field. The transformation from PAS to the rotor-fixed frame is expressed by the Euler angles $(\alpha_{\mathrm{PR}},\beta_{\mathrm{PR}},\gamma_{\mathrm{PR}})$, for which we use the Rose's definition.[14] The transformation from the rotor-fixed frame to the laboratory frame is described by $(\omega_r t,\theta,0)$, where ω_r is the angular velocity of sample spinning and θ is the angle between the z^{rot} axis and the z^{lab} axis. The time-dependent Hamiltonian of a spin packet in the rotating frame is written as[1]

$$H(t)=\omega_0[\bar{\sigma}-\Delta+\sigma_{C1}\cos(\gamma_{\mathrm{PR}}+\omega_r t)+\sigma_{S1}\sin(\gamma_{\mathrm{PR}}+\omega_r t)+\sigma_{C2}\cos 2(\gamma_{\mathrm{PR}}+\omega_r t)+\sigma_{S2}\sin 2(\gamma_{\mathrm{PR}}+\omega_r t)]I_z, \quad (1)$$

with

$$\bar{\sigma}=\sigma^{\mathrm{iso}}+P_2(\cos\theta)[P_2(\cos\beta_{\mathrm{PR}})(\sigma_{zz}^{\mathrm{PAS}}-\sigma^{\mathrm{iso}})+\tfrac{1}{2}\sin^2\beta_{\mathrm{PR}}\cos 2\alpha_{\mathrm{PR}}(\sigma_{xx}^{\mathrm{PAS}}-\sigma_{yy}^{\mathrm{PAS}})], \quad (2)$$

$$\sigma_{C1}=\sin\theta\cos\theta\sin\beta_{\mathrm{PR}}\cos\beta_{\mathrm{PR}}[-3(\sigma_{zz}^{\mathrm{PAS}}-\sigma^{\mathrm{iso}})+\cos 2\alpha_{\mathrm{PR}}(\sigma_{xx}^{\mathrm{PAS}}-\sigma_{yy}^{\mathrm{PAS}})], \quad (3)$$

$$\sigma_{S1}=-\sin\theta\cos\theta\sin\beta_{\mathrm{PR}}\sin 2\alpha_{\mathrm{PR}}(\sigma_{xx}^{\mathrm{PAS}}-\sigma_{yy}^{\mathrm{PAS}}), \quad (4)$$

$$\sigma_{C2}=\tfrac{1}{4}\sin^2\theta[3\sin^2\beta_{\mathrm{PR}}(\sigma_{zz}^{\mathrm{PAS}}-\sigma^{\mathrm{iso}})+(1+\cos^2\beta_{\mathrm{PR}})\cos 2\alpha_{\mathrm{PR}}(\sigma_{xx}^{\mathrm{PAS}}-\sigma_{yy}^{\mathrm{PAS}})], \quad (5)$$

$$\sigma_{S2}=-\tfrac{1}{2}\sin^2\theta\cos\beta_{\mathrm{PR}}\sin 2\alpha_{\mathrm{PR}}(\sigma_{xx}^{\mathrm{PAS}}-\sigma_{yy}^{\mathrm{PAS}}), \quad (6)$$

$$\sigma^{\mathrm{iso}}=\frac{\sigma_{xx}^{\mathrm{PAS}}+\sigma_{yy}^{\mathrm{PAS}}+\sigma_{zz}^{\mathrm{PAS}}}{3}, \quad (7)$$

where ω_0 is the resonance frequency, Δ is the resonance offset, and $\sigma_{ii}^{\mathrm{PAS}}$ $(i=x,y,z)$ is the ii element of the CSA tensor in PAS. This Hamiltonian can be rewritten as

$$H(t)=\omega_0[\bar{\sigma}-\Delta+\sigma_1\cos(\omega_r t+\gamma_{\mathrm{PR}}+\delta_1)+\sigma_2\cos 2(\omega_r t+\gamma_{\mathrm{PR}}+\delta_2)]I_z, \quad (8)$$

where

$$\sigma_1=\sqrt{\sigma_{C1}^2+\sigma_{S1}^2}, \quad (9)$$

with

$$\tan\delta_1=-\frac{\sigma_{S1}}{\sigma_{C1}}, \quad (10)$$

and

$$\sigma_2=\sqrt{\sigma_{C2}^2+\sigma_{S2}^2}, \quad (11)$$

with

$$\tan 2\delta_2=-\frac{\sigma_{S2}}{\sigma_{C2}}. \quad (12)$$

We assume that the symmetry axis of a uniaxially oriented sample is aligned parallel to the spinning axis. The angles α_{PR} and β_{PR} then represent the azimuthal and polar angles of the symmetry axis in PAS, respectively. We also assume for the present that α_{PR} and β_{PR} have definite values, causing no line broadening even in a static sample. The other angle γ_{PR}, being uniformly distributed from 0 to 2π, broadens the line in static samples; in rotating samples, the broadening is averaged out and a sharp center band appears at $\bar{\sigma}$. Note that the sharp peak is observed at $\bar{\sigma}$ even in a static sample $(\omega_r=0)$, when θ is set to 0; i.e., the symmetry axis is aligned parallel to the magnetic field direction. When θ deviates from the magic angle θ_m (OMAS), $\bar{\sigma}$ contains information on CSA. However, knowledge of $\bar{\sigma}$ and σ^{iso} is not enough to determine the three principal values. For obtaining complementary information on CSAs, we propose some methods to determine σ_2 by observing another sharp line.

We recently reported[7] that the sharp peak at σ_2 can be obtained by a new transformation of the FID for a static uniaxially oriented sample with the symmetry axis aligned perpendicular to the magnetic field $(\theta=\pi/2)$, if the Δ term cancels out the $\bar{\sigma}$ term by adjusting the rf frequency, i.e., $\Delta=\bar{\sigma}$: in this case, the Hamiltonian is written as

$$H^{\mathrm{GET}}=\omega_0\sigma_2 I_z\cos 2(\gamma_{\mathrm{PR}}+\delta_2). \quad (13)$$

The FID $M(t)$ observed under this Hamiltonian is purely amplitude modulated:

$$M(t)=M(0)J_0(\omega_0\sigma_2 t), \quad (14)$$

where $J_0(x)$ is the zeroth-order Bessel function of the first kind.[15] FT of $M(t)$ provides a powder pattern due to the distribution of γ_{PR}, while $M(t)$ can be transformed into a sharp line at σ_2 by GET.[7]

In order to enable this approach to be applied to systems with more than one distinct $\bar{\sigma}$ value, we must remove the above restriction on Δ. Thus, we try to obtain pulse sequences under which the time evolution of a spin system can be described by the average Hamiltonian proportional to H^{GET}:

$$\bar{H}=\omega_0\mu\sigma_2 I_z\cos 2(\gamma_{PR}+\delta_2), \tag{15}$$

where μ is the scaling factor. GET then provides a sharp line at $\mu\sigma_2$ even if $\bar{\sigma}-\Delta\neq 0$. Tycko *et al.* proposed unequally spaced rotor-synchronous π pulse trains in order to reintroduce the CSA powder patterns in a polycrystalline sample under MAS, by which both the σ_1 and σ_2 terms are simultaneously reintroduced into the average Hamiltonian.[16] On the analogy of the sequences of Tycko *et al.*, we try to design rotor-synchronous π pulse trains which prevent only the σ_2 term from being time averaged by sample spinning for realizing the average Hamiltonian given by Eq. (15).

We assume that δ-function π pulses are irradiated at τ_k $(k=1,2,\ldots,n)$ within each spinning period from $\tau_0=0$ to $\tau_{n+1}=\tau_r$, where $\tau_r=2\pi/\omega_r$ is the cycle time of sample spinning. In order to fulfill the cyclic condition, n must be an even number. The zeroth-order average Hamiltonian can easily be calculated by the average Hamiltonian theory:[1,2]

$$\begin{aligned}\bar{H}=\omega_0(\bar{\sigma}-\Delta)I_z+\omega_0\sum_{k=1}^{n/2}\Bigg\{&\frac{2(\bar{\sigma}-\Delta)(\tau_{2k-1}-\tau_{2k})}{\tau_r}\\&+\frac{\sigma_1}{\pi}[\sin(\omega_r\tau_{2k-1}+\gamma_{PR}+\delta_1)-\sin(\omega_r\tau_{2k}+\gamma_{PR}+\delta_1)]\\&+\frac{\sigma_2}{2\pi}[\sin 2(\omega_r\tau_{2k-1}+\gamma_{PR}+\delta_2)\\&-\sin 2(\omega_r\tau_{2k}+\gamma_{PR}+\delta_2)]\Bigg\}I_z.\end{aligned} \tag{16}$$

Equating Eq. (15) to Eq. (16), we obtain the following conditions:

$$\sum_{k=1}^{n/2}\frac{2(\tau_{2k-1}-\tau_{2k})}{\tau_r}=-1, \tag{17}$$

$$\sum_{k=1}^{n/2}[\sin(\omega_r\tau_{2k-1}+\gamma_{PR}+\delta_1)-\sin(\omega_r\tau_{2k}+\gamma_{PR}+\delta_1)]=0, \tag{18}$$

and

$$\begin{aligned}\sum_{k=1}^{n/2}\frac{1}{2\pi}&[\sin 2(\omega_r\tau_{2k-1}+\gamma_{PR}+\delta_2)-\sin 2(\omega_r\tau_{2k}+\gamma_{PR}+\delta_2)]\\&=\mu\cos 2(\gamma_{PR}+\delta_2).\end{aligned} \tag{19}$$

For the simplest case, i.e., $n=2$, Eq. (18) cannot be satisfied. For the next simplest case, i.e., $n=4$, we obtain the solution

$$(\tau_1,\tau_2,\tau_3,\tau_4)=\left(\frac{1}{8}\tau_r,\frac{3}{8}\tau_r,\frac{5}{8}\tau_r,\frac{7}{8}\tau_r\right), \tag{20}$$

with the scaling factor

$$\mu=\frac{2}{\pi}. \tag{21}$$

Thus, when a π pulse is irradiated at the center of each quarter rotor cycle, the FID observed every rotor cycle can be transformed into a sharp line at $\mu\sigma_2$ by GET. We treat this simplest sequence in the following, and refer to this pulse sequence simply as π pulse train (PPT).

The above results are obtained for ideal δ-function π pulses. Here we evaluate the effectiveness of various phase cycling schemes in compensation for finite pulse width, rf-amplitude missetting, and resonance offset. We separate the Hamiltonian into two parts:

$$H(t)=H_0(t)+H_1(t). \tag{22}$$

The $H_0(t)$ term includes the effect of rf-amplitude missetting and resonance offset:

$$\begin{aligned}H_0(t)=\omega_0[&\bar{\sigma}-\Delta+\sigma_1\cos(\omega_r t+\gamma_{PR}+\delta_1)\\&+\sigma_2\cos 2(\omega_r t+\gamma_{PR}+\delta_2)]I_z+\Delta_{rf}(\phi,t),\end{aligned} \tag{23}$$

with

$$\Delta_{rf}(\phi,t)=\begin{cases}0 & \text{during the pulse interval,}\\ \dfrac{\delta_{rf}}{\tau_p}I_\phi & \text{during the pulse irradiation,}\end{cases} \tag{24}$$

where ϕ is the phase of the π pulse, τ_p is the π pulse width, and δ_{rf} is the deviation of the nutation angle from π. The $H_1(t)$ term is written as

$$H_1(t)=\begin{cases}0 & \text{during the pulse interval,}\\ \dfrac{\pi}{\tau_p}I_\phi & \text{during the pulse irradiation.}\end{cases} \tag{25}$$

We assume that π pulses with finite width are centered at τ_k $(k=1,2,3,4)$. Using the interaction representation with respect to $H_1(t)$, we can calculate the zeroth-order average Hamiltonian for PPT. The average Hamiltonians obtained for various phase cycling schemes[17–19] are listed in Table I, where d is the duty factor of π pulses: $d=4\tau_p/\tau_r$ in the present case. The average Hamiltonians for the phase cycling schemes except for XXXX and $X\bar{X}\bar{X}X$ do not include the terms of rf-amplitude missetting and resonance offset. For finite pulse width, only the average Hamiltonian for $X\bar{X}\bar{X}XX\bar{X}\bar{X}X$, $XYXY\bar{X}\bar{Y}\bar{X}\bar{Y}$, MLEV16 (Ref. 17), or XY16 (Ref. 19) has the required form of Eq. (15) with the scaling factor μ:

$$\mu=\frac{2}{\pi}\frac{1}{1-d^2}\cos\left(\frac{\pi}{2}d\right). \tag{26}$$

FID signals observed by PPT with any of the four phase cycling schemes are transformed into γ-encoded spectra by GET. Hereafter, the combination of PPT and GET is referred to as PPT–GET. The phase cycling schemes of XXXXXXXX and XYXYXYXY are preferable to MLEV16

TABLE I. Average Hamiltonians for PPT ($n=4$) under various phase cycling schemes.

Phase cycling scheme	Average Hamiltonian
XXXX	$\bar{H}_0=\delta_{\rm rf}I_x\frac{4}{\tau_r}+\omega_0\sigma_2\frac{2}{\pi}\frac{1}{1-d^2}\cos\left(\frac{\pi}{2}d\right)\times[-I_y d\sin 2(\gamma_{\rm PR}+\delta_2)+I_z\cos 2(\gamma_{\rm PR}+\delta_2)]$
$\mathrm{X\bar{X}\bar{X}X}$	$\bar{H}_0=\omega_0\bar{\sigma}I_y\frac{2}{\pi}d+\omega_0\sigma_2 I_z\frac{2}{\pi}\frac{1}{1-d^2}\cos\left(\frac{\pi}{2}d\right)\times\cos 2(\gamma_{\rm PR}+\delta_2)$
MLEV4[a]/XY4[b]	$\bar{H}_0=\omega_0\sigma_1 I_y\frac{\sqrt{2}d}{\pi}\left(1-\frac{d^2}{4}\right)^{-1}\times\cos\left(\frac{\pi}{4}d\right)\cos(\gamma_{\rm PR}+\delta_1)+\omega_0\sigma_2 I_z\frac{2}{\pi}\frac{1}{1-d^2}\times\cos\left(\frac{\pi}{2}d\right)\cos 2(\gamma_{\rm PR}+\delta_2)$
MLEV8[a]	$\bar{H}_0=\omega_0\sigma_1 I_y\frac{d}{\pi}\left(1-\frac{d^2}{4}\right)^{-1}\cos\frac{\pi}{4}d\times\sin\left(\gamma_{\rm PR}+\frac{\pi}{4}+\delta_1\right)+\omega_0\sigma_2 I_z\frac{2}{\pi}\frac{1}{1-d^2}\times\cos\frac{\pi}{2}d\cos 2(\gamma_{\rm PR}+\delta_2)$
XY8[c]	$\bar{H}_0=\omega_0\sigma_1(I_x-I_y)\frac{\sqrt{2}d}{\pi}\left(1-\frac{d^2}{4}\right)^{-1}\times\cos\left(\frac{\pi}{4}d\right)\sin(\gamma_{\rm PR}+\delta_1)+\omega_0\sigma_2 I_z\frac{2}{\pi}\frac{1}{1-d^2}\cos\left(\frac{\pi}{2}d\right)\cos 2(\gamma_{\rm PR}+\delta_2)$
$\mathrm{XX\overline{XXXXXX}X}$[d]/ XYXY$\overline{\mathrm{XYXY}}$/ MLEV16[a]/XY16[c]	$\bar{H}_0=\omega_0\sigma_2 I_z\frac{2}{\pi}\frac{1}{1-d^2}\cos\frac{\pi}{2}d\cos 2(\gamma_{\rm PR}+\delta_2)$

[a]Reference 17.
[b]Reference 18.
[c]Reference 19.
[d]Reference 16.

and XY16, because the former yield less cycling sidebands.[20] When the spinning axis is perpendicular to the magnetic field ($\theta=\pi/2$) or one of the PAS axes is parallel to the symmetry axis, the σ_1 term vanishes, and therefore MLEV4 (Ref. 17) and XY4 (Ref. 18), which have a further shorter cycle time, can be used. The sequences of Tycko *et al.* can also be used under this condition to realize $\sigma_1=0$. However, even the largest scaling factor in the sequences of Tycko *et al.*, which is 0.394 for $d=0$ in the four pulse version, is smaller than that for PPT [Eq. (26)].

When $d\neq 0$, the average Hamiltonian for PPT under the XXXX phase cycling scheme does not have the required form of Eq. (15), so that we cannot obtain γ-encoded spectra by GET. For the windowless limit, i.e., $d=1$, PPT with XXXX is identical to rotary resonance recoupling (R^3) with the rf-field strength twice the spinning frequency,[21] and the average Hamiltonian for R^3 can be obtained in the limit of the average Hamiltonian for PPT with XXXX when d approaches 1:

$$\bar{H}_0=\delta_{\rm rf}I_x\frac{4}{\tau_r}+\omega_0\mu\sigma_2[-I_y\sin 2(\gamma_{\rm PR}+\delta_2)+I_z\cos 2(\gamma_{\rm PR}+\delta_2)], \tag{27}$$

with

$$\mu=\tfrac{1}{2}. \tag{28}$$

This Hamiltonian shows the resonance frequency to be independent of $\gamma_{\rm PR}$. In the case of $\delta_{\rm rf}=0$, R^3 is already known to be γ-encoded.[21] The present result shows that it is true also for $\delta_{\rm rf}\neq 0$. The other PPT sequences are not γ-encoded, even if $d=1$. Note that the spectrum observed by R^3 is very sensitive to rf-amplitude missetting, since the average Hamiltonian in Eq. (27) includes $\delta_{\rm rf}$ at zeroth order as previously reported for heteronuclear dipolar recoupling by R^3.[22]

In order to compensate for rf-field inhomogeneity, we replace the π pulses 180_0 in PPT with the composite inversion pulses $90_{270}180_0 90_{270}$.[23] We refer to this new sequence as the composite inversion pulse train (CIPT). The average Hamiltonians obtained for CIPT with various phase cycling schemes are listed in Table II. Since τ_p represents the length of a conventional π pulse, d is given by $8\tau_p/\tau_r$. Table II shows that the phase cycling schemes of $\mathrm{XXXXXXXX}$, XYXY$\overline{\mathrm{XYXY}}$, MLEV16, and XY16 give the required average Hamiltonian [Eq. (15)] with the scaling factor

$$\mu=\frac{2}{\pi}\left[1-\left(\frac{d}{2}\right)^2\right]^{-1}\left[\cos\left(\frac{\pi}{2}d\right)+\frac{d}{2}\sin\left(\frac{\pi}{4}d\right)\right]. \tag{29}$$

γ-encoded spectra can be obtained by the combination of CIPT with one of these phase cycling schemes and GET, to which we refer as CIPT–GET.

As well as PPT, CIPT can be a γ-encoded sequence only in the windowless limit with XXXX, and the average Hamiltonian is given by

$$\bar{H}_0=\omega_0\mu\sigma_2[-I_y\sin 2(\gamma_{\rm PR}+\delta_2)+I_z\cos 2(\gamma_{\rm PR}+\delta_2)], \tag{30}$$

with

$$\mu=\frac{2\sqrt{2}}{3\pi}. \tag{31}$$

We refer to this sequence as the composite inversion rotary-resonance recoupling (CIR^3); the rotary resonance condition is given by $\omega_1=4\omega_r$. Note that no term including $\delta_{\rm rf}$ appears in this average Hamiltonian contrary to R^3, so that the CIR^3 sequence is expected to be less sensitive to rf-field inhomogeneity than R^3.

Thus, one can remove the line-broadening due to distribution of the angle $\gamma_{\rm PR}$, using one of the above methods, i.e., PPT–GET, CIPT–GET, R^3, and CIR^3. Sharp peaks appear in the γ-encoded spectra of uniaxially oriented samples, when they have unique values for $\alpha_{\rm PR}$ and $\beta_{\rm PR}$. However, when $\alpha_{\rm PR}$ and $\beta_{\rm PR}$ are more or less distributed, γ-encoded spectra show broadened peaks. If we observe the 2D spectrum in which peaks appear at σ_2 in one dimension and $\bar{\sigma}$ in the other dimension under OMAS, the distribution of the $\alpha_{\rm PR}$

TABLE II. Average Hamiltonians for CIPT ($n=4$) under various phase cycling schemes.

Phase cycling scheme	Average Hamiltonian
XXXX	$\bar{H}_0=-\omega_0\sigma_2 I_y\frac{2}{\pi}\left[1-\left(\frac{d}{2}\right)^2\right]^{-1}\frac{d}{2}\cos\left(\frac{\pi}{4}d\right)\sin 2(\gamma_{PR}+\delta_2)+\omega_0\sigma_2 I_z\frac{2}{\pi}\left[1-\left(\frac{d}{2}\right)^2\right]^{-1}\left[\cos\left(\frac{\pi}{2}d\right)+\frac{d}{2}\sin\left(\frac{\pi}{4}d\right)\right]\cos 2(\gamma_{PR}+\delta_2)$
$X\bar{X}X\bar{X}$	$\bar{H}_0=\omega_0\sigma_2\frac{2}{\pi}\left[1-\left(\frac{d}{2}\right)^2\right]^{-1}\left\{I_x\frac{d}{2}\sin\left(\frac{\pi}{2}d\right)+I_z\left[\cos\left(\frac{\pi}{2}d\right)+\frac{d}{2}\sin\left(\frac{\pi}{4}d\right)\right]\right\}\cos 2(\gamma_{PR}+\delta_2)+\omega_0\bar{\sigma}I_y\frac{d}{\pi}$
MLEV4[a]	$\bar{H}_0=\omega_0\sigma_1\frac{d}{\sqrt{2}\pi}\left[1-\left(\frac{d}{4}\right)^2\right]^{-1}\left[I_x\sin\left(\frac{\pi}{4}d\right)+I_y\cos\left(\frac{\pi}{8}d\right)\right]\cos(\gamma_{PR}+\delta_1)+\omega_0\sigma_2 I_z\frac{2}{\pi}\left[1-\left(\frac{d}{2}\right)^2\right]^{-1}\left[\cos\left(\frac{\pi}{2}d\right)+\frac{d}{2}\sin\left(\frac{\pi}{4}d\right)\right]\cos 2(\gamma_{PR}+\delta_2)$
XY4[b]	$\bar{H}_0=\omega_0\sigma_1\frac{d}{2\pi}\left[1-\left(\frac{d}{4}\right)^2\right]^{-1}\left\{I_x\left[\sin\left(\frac{\pi}{4}d\right)+\cos\left(\frac{\pi}{8}d\right)\right]+I_y\left[-\sin\left(\frac{\pi}{4}d\right)+\cos\left(\frac{\pi}{8}d\right)\right]\right\}\times\sin\left(\gamma_{PR}+\frac{\pi}{4}+\delta_1\right)+\omega_0\sigma_2 I_z\frac{2}{\pi}\left[1-\left(\frac{d}{2}\right)^2\right]^{-1}\left[\cos\left(\frac{\pi}{2}d\right)+\frac{d}{2}\sin\left(\frac{\pi}{4}d\right)\right]\cos 2(\gamma_{PR}+\delta_2)$
MLEV8[a]	$\bar{H}_0=\omega_0\sigma_1\frac{d}{2\pi}\left[1-\left(\frac{d}{4}\right)^2\right]^{-1}\left[I_x\sin\left(\frac{\pi}{4}d\right)+I_y\cos\left(\frac{\pi}{8}d\right)\right]\sin\left(\gamma_{PR}+\frac{\pi}{4}+\delta_1\right)+\omega_0\sigma_2 I_z\frac{2}{\pi}\left[1-\left(\frac{d}{2}\right)^2\right]^{-1}\times\left[\cos\left(\frac{\pi}{2}d\right)+\frac{d}{2}\sin\left(\frac{\pi}{4}d\right)\right]\cos 2(\gamma_{PR}+\delta_2)$
XY8[c]	$\bar{H}_0=\omega_0\sigma_1\frac{\sqrt{2}d}{4\pi}\left[1-\left(\frac{d}{4}\right)^2\right]^{-1}\left\{\left[\sin\left(\frac{\pi}{4}d\right)+\cos\left(\frac{\pi}{8}d\right)\right]I_x+\left[\sin\left(\frac{\pi}{4}d\right)-\cos\left(\frac{\pi}{8}d\right)\right]I_y\right\}\times\sin\left(\gamma_{PR}+\frac{\pi}{4}+\delta_1\right)+\omega_0\sigma_2 I_z\frac{2}{\pi}\left[1-\left(\frac{d}{2}\right)^2\right]^{-1}\times\left[\cos\left(\frac{\pi}{2}d\right)+\frac{d}{2}\sin\left(\frac{\pi}{4}d\right)\right]\cos 2(\gamma_{PR}+\delta_2)$
$X\overline{XXXXXX}X$[d]/ XYXY$\overline{XYXY}$/ MLEV16[a]/XY16[c]	$\bar{H}_0=\omega_0\sigma_2 I_z\frac{2}{\pi}\left[1-\left(\frac{d}{2}\right)^2\right]^{-1}\left[\cos\left(\frac{\pi}{2}d\right)+\frac{d}{2}\sin\left(\frac{\pi}{4}d\right)\right]\cos 2(\gamma_{PR}+\delta_2)$

[a]Reference 17.
[b]Reference 18.
[c]Reference 19.
[d]Reference 16.

and β_{PR} angles broadens the peaks in both dimensions. Here, we calculate the $\sigma_2/\bar{\sigma}$ 2D powder pattern, and then we propose a method to obtain the α_{PR} and β_{PR} distribution directly from the 2D powder pattern.

We define PAS to satisfy the following condition in the rest of this section without loss of generality:

$$P_2(\cos\theta)\sigma_{zz}^{PAS}\geqslant P_2(\cos\theta)\sigma_{yy}^{PAS}\geqslant P_2(\cos\theta)\sigma_{xx}^{PAS}. \quad (32)$$

Under this condition $\bar{\sigma}$ reaches the minimum value $\bar{\sigma}_{min}$ when $\cos\beta_{PR}=0$ and $\cos 2\alpha_{PR}=1$ [see Eq. (2)], since $P_2(\cos\theta)(\sigma_{zz}^{PAS}-\sigma^{iso})\geqslant 0$ and $P_2(\cos\theta)(\sigma_{xx}^{PAS}-\sigma_{yy}^{PAS})\leqslant 0$,

$$\bar{\sigma}_{min}=\sigma^{iso}+P_2(\cos\theta)(\sigma_{xx}^{PAS}-\sigma^{iso}), \quad (33)$$

and $\bar{\sigma}$ has the maximum value $\bar{\sigma}_{max}$ when $|\cos\beta_{PR}|=1$:

$$\bar{\sigma}_{max}=\sigma^{iso}+P_2(\cos\theta)(\sigma_{zz}^{PAS}-\sigma^{iso}). \quad (34)$$

First, we obtain the $\sigma_2/\bar{\sigma}$ 2D powder pattern due to uniform distribution of α_{PR} and $\sin\beta_{PR}$. From Eqs. (2), (5), (6), and (11), we obtain the following relationship:

$$\left(\frac{\bar{\sigma}-\sigma^{iso}}{2P_2(\cos\theta)}+\sigma_{zz}^{PAS}-\sigma^{iso}\right)^2-\left(\frac{\sigma_2}{\sin^2\theta}\right)^2=\cos^2\beta_{PR}(\sigma_{zz}^{PAS}-\sigma_{xx}^{PAS})(\sigma_{zz}^{PAS}-\sigma_{yy}^{PAS}). \quad (35)$$

This equation shows that the trajectory of $(\sigma_2,\bar{\sigma})$ for fixed β_{PR} is a hyperbolic curve. Since $\cos^2\beta_{PR}(\sigma_{zz}^{PAS}-\sigma_{xx}^{PAS})\times(\sigma_{zz}^{PAS}-\sigma_{yy}^{PAS})>0$, the focal axis of the hyperbola is parallel to the $\bar{\sigma}$ axis. The $\sigma_2/\bar{\sigma}$ 2D peak appears on the hyperbola branch open toward the positive-$\bar{\sigma}$ direction, because $\bar{\sigma}_{min}\geqslant\sigma^{iso}-2P_2(\cos\theta)(\sigma_{zz}^{PAS}-\sigma^{iso})$. A few hyperbolas for different β_{PR} are shown by dotted curves in Scheme 1:

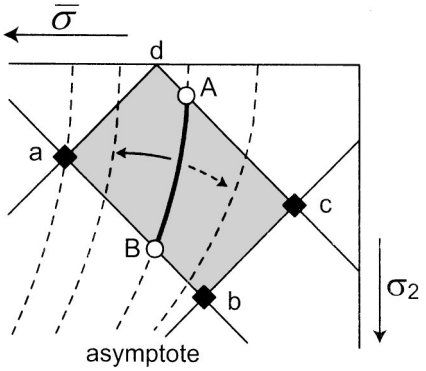

For a fixed $\beta_{PR}=\beta_{AB}$, $\bar{\sigma}(\cos 2\alpha_{PR},\beta_{AB})$ takes the minimum $\bar{\sigma}(1,\beta_{AB})$ (A) and the maximum $\bar{\sigma}(-1,\beta_{AB})$ (B), when $\cos 2\alpha_{PR}=1$ and -1, respectively. Resonances appear on the hyperbola $\widehat{AB}$ represented by the bold curve in Scheme 1. As increasing $|\cos\beta_{PR}|$, the hyperbola moves toward the solid arrow direction. With decreasing $|\cos\beta_{PR}|$, the hyperbolic curve approaches the asymptote bc toward the dotted arrow direction. When $\cos\beta_{PR}=0$, the curve is coincident with the asymptote given by

$$\sigma_2=\left|\frac{\sin^2\theta}{2P_2(\cos\theta)}\right|[\bar{\sigma}-\sigma^{iso}+2P_2(\cos\theta)(\sigma_{zz}^{PAS}-\sigma^{iso})]. \quad (36)$$

The trajectories of $\bar{\sigma}(1,\beta_{PR})$ and $\bar{\sigma}(-1,\beta_{PR})$ for variable β_{PR} are obtained by substituting $\cos 2\alpha_{PR}=\pm 1$ into Eqs. (2), (5), (6), and (11) and considering $\bar{\sigma}\leqslant\bar{\sigma}_{max}$:

$$\sigma_2 = \sin^2\theta \left| -\frac{\overline{\sigma} - \sigma^{\mathrm{iso}}}{2P_2(\cos\theta)} - (\sigma_{yy}^{\mathrm{PAS}} - \sigma^{\mathrm{iso}}) \right| \tag{37}$$

for $\overline{\sigma}(1,\beta_{\mathrm{PR}})$ and

$$\sigma_2 = -\left| \frac{\sin^2\theta}{2P_2(\cos\theta)} \right| [\overline{\sigma} - \sigma^{\mathrm{iso}} + 2P_2(\cos\theta)(\sigma_{xx}^{\mathrm{PAS}} - \sigma^{\mathrm{iso}})] \tag{38}$$

for $\overline{\sigma}(-1,\beta_{\mathrm{PR}})$. These equations show that the trajectories of $\overline{\sigma}(1,\beta_{\mathrm{PR}})$ and $\overline{\sigma}(-1,\beta_{\mathrm{PR}})$ are represented by the bent line cda and the line ab, respectively, in Scheme 1. Thus, when the orientations α_{PR} and $\sin\beta_{\mathrm{PR}}$ are uniformly distributed, the resonances cover over the parallelogram region □abcd enclosed with the four lines given by Eqs. (36)–(38), and resonances with any orientations appear only within the parallelogram.

Here, we show how to obtain the orientation distribution $p(\alpha_{\mathrm{PR}},\beta_{\mathrm{PR}})$ from the spectral intensity $S(\sigma_2,\overline{\sigma})$. Since the hyperbolas for different $|\cos\beta_{\mathrm{PR}}|$ never intercross each other, the one-to-one correspondence between a spectral point $(\sigma_2,\overline{\sigma})$ and an orientation $(\alpha_{\mathrm{PR}},\beta_{\mathrm{PR}})$ is established by Eqs. (2) and (35). Thus, when the principal values of the CSA tensor are known, we can directly obtain $p(\alpha_{\mathrm{PR}},\beta_{\mathrm{PR}})$ from $S(\sigma_2,\overline{\sigma})$:[2]

$$S(\sigma_2,\overline{\sigma}) = \frac{p(\alpha_{\mathrm{PR}},\beta_{\mathrm{PR}})}{\partial(\sigma_2,\overline{\sigma})/\partial(\alpha_{\mathrm{PR}},\cos\beta_{\mathrm{PR}})}, \tag{39}$$

where $\partial(\sigma_2,\overline{\sigma})/\partial(\alpha_{\mathrm{PR}},\cos\beta_{\mathrm{PR}})$ is the Jacobian determinant. Note that there are degeneracies for α_{PR}, $\alpha_{\mathrm{PR}}+\pi$, $2\pi-\alpha_{\mathrm{PR}}$, and $\pi-\alpha_{\mathrm{PR}}$ and for β_{PR} and $\pi-\beta_{\mathrm{PR}}$. We can represent the distributions uniquely by limiting the ranges of α_{PR} and β_{PR} to $0\leqslant\alpha_{\mathrm{PR}}<\pi/2$ and $0\leqslant\beta_{\mathrm{PR}}<\pi/2$:

$$\begin{aligned} P(\alpha_{\mathrm{PR}},\beta_{\mathrm{PR}}) = {} & p(\alpha_{\mathrm{PR}},\beta_{\mathrm{PR}}) + p(\alpha_{\mathrm{PR}}+\pi,\beta_{\mathrm{PR}}) \\ & + p(2\pi-\alpha_{\mathrm{PR}},\beta_{\mathrm{PR}}) + p(\pi-\alpha_{\mathrm{PR}},\beta_{\mathrm{PR}}) \\ & + p(\alpha_{\mathrm{PR}},\pi-\beta_{\mathrm{PR}}) + p(\alpha_{\mathrm{PR}}+\pi,\pi-\beta_{\mathrm{PR}}) \\ & + p(2\pi-\alpha_{\mathrm{PR}},\pi-\beta_{\mathrm{PR}}) \\ & + p(\pi-\alpha_{\mathrm{PR}},\pi-\beta_{\mathrm{PR}}). \end{aligned} \tag{40}$$

The Jacobian determinant vanishes either when $\cos\beta_{\mathrm{PR}}=0$ and $\cos 2\alpha_{\mathrm{PR}}=\pm 1$ or when $|\cos\beta_{\mathrm{PR}}|=1$; i.e., one PAS axis is parallel to the z^{rot} axis. Thus, three singularity appears at $(\sigma_2,\overline{\sigma})=[1/2\sin^2\theta\cdot|\sigma_{xx}^{\mathrm{PAS}}-\sigma_{yy}^{\mathrm{PAS}}|,\sigma^{\mathrm{iso}}+P_2(\cos\theta)(\sigma_{zz}^{\mathrm{PAS}}-\sigma^{\mathrm{iso}})]$, $[1/2\sin^2\theta\cdot|\sigma_{zz}^{\mathrm{PAS}}-\sigma_{xx}^{\mathrm{PAS}}|,\sigma^{\mathrm{iso}}+P_2(\cos\theta)(\sigma_{yy}^{\mathrm{PAS}}-\sigma^{\mathrm{iso}})]$, and $[1/2\sin^2\theta\cdot|\sigma_{yy}^{\mathrm{PAS}}-\sigma_{zz}^{\mathrm{PAS}}|,\sigma^{\mathrm{iso}}+P_2(\cos\theta)(\sigma_{xx}^{\mathrm{PAS}}-\sigma^{\mathrm{iso}})]$, which coincide with points a, b, and c, respectively, in Scheme 1.

When the CSA tensor is axially symmetric, the $\sigma_2/\overline{\sigma}$ plot appears on the straight line given by Eq. (38) for $\sigma_{xx}^{\mathrm{PAS}}=\sigma_{yy}^{\mathrm{PAS}}$ and Eq. (36) for $\sigma_{yy}^{\mathrm{PAS}}=\sigma_{zz}^{\mathrm{PAS}}$. We can determine the value of $\sigma^{\mathrm{iso}}-2P_2(\cos\theta)(\sigma_{yy}^{\mathrm{PAS}}-\sigma^{\mathrm{iso}})$ from the point d, $(\sigma_2,\overline{\sigma})=(\sigma^{\mathrm{iso}}-2P_2(\cos\theta)(\sigma_{yy}^{\mathrm{PAS}}-\sigma^{\mathrm{iso}}),0)$, where $\sigma_{yy}^{\mathrm{PAS}}$ represents the CSA component perpendicular to the tensor symmetry axis. Since the resonance position for the axially symmetric CSA does not depend on α_{PR} but on $|\cos\beta_{\mathrm{PR}}|$ as shown by Eq. (2), the distribution of $|\cos\beta_{\mathrm{PR}}|$, i.e., $P(\beta_{\mathrm{PR}})$, can directly be obtained from the spectral intensity:

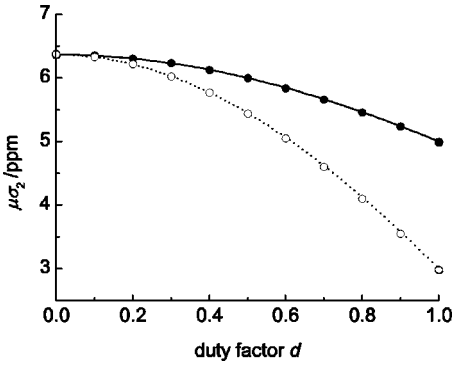

FIG. 1. Duty factor dependence of a CSA parameter $\mu\sigma_2$ calculated for PPT–GET (●, solid line) and CIPT–GET (○, dotted line) under MAS. In the calculations, the chemical shift tensor of $(\sigma_{xx}^{\mathrm{PAS}},\sigma_{yy}^{\mathrm{PAS}},\sigma_{zz}^{\mathrm{PAS}})=(-30,\ 0,\ 30)$ ppm with z^{PAS} parallel to the symmetry axis of a uniaxially oriented sample [$\sigma_2=10$ ppm from Eq. (11)] was used. The rf field was assumed to be irradiated at $\overline{\sigma}$. A spinning frequency of 2.00 kHz and a Larmor frequency of 75 MHz were used. The rf-field inhomogeneity was neglected ($\delta_{\mathrm{rf}}=0$). The lines were obtained from the theoretical scaling factor μ given in Eq. (26) for PPT–GET and Eq. (29) for CIPT–GET using the σ_2 value of 10 ppm. The circles represent the $\mu\sigma_2$ values obtained from spectra numerically calculated by the multistep method.

$$P(\beta_{\mathrm{PR}}) = S(\sigma')\frac{\partial\sigma'}{\partial\cos\beta_{\mathrm{PR}}}, \tag{41}$$

with

$$P(\beta_{\mathrm{PR}}) = \frac{2}{\pi}\int_0^{\pi/2} d\alpha_{\mathrm{PR}} P(\alpha_{\mathrm{PR}},\beta_{\mathrm{PR}}), \tag{42}$$

where the σ' axis is parallel to the line $\sigma_2=-|\sin^2\theta/2P_2(\cos\theta)|\overline{\sigma}$ for $\sigma_{xx}^{\mathrm{PAS}}=\sigma_{yy}^{\mathrm{PAS}}$ and $\sigma_2=|\sin^2\theta/2P_2(\cos\theta)|\overline{\sigma}$ for $\sigma_{yy}^{\mathrm{PAS}}=\sigma_{zz}^{\mathrm{PAS}}$.

III. NUMERICAL CALCULATIONS

Using the multistep method, we numerically calculated γ-encoded spectra of a uniaxially oriented sample which are observed by R^3, CIR^3, PPT–GET, and CIPT–GET under MAS. In the calculations a chemical shift tensor of $(\sigma_{xx}^{\mathrm{PAS}},\sigma_{yy}^{\mathrm{PAS}},\sigma_{zz}^{\mathrm{PAS}})=(-30,0,30)$ ppm with the z^{PAS} axis parallel to the spinning axis ($\beta_{\mathrm{PR}}=0$) with $\omega_{\mathrm{r}}/2\pi=2$ kHz was used. Under the conditions, σ_2 is 10 ppm from Eqs. (5), (6), and (11). The rf field was assumed to be irradiated at $\overline{\sigma}$ ($\Delta=\overline{\sigma}$).

First, we calculated γ-encoded spectra, assuming $\delta_{\mathrm{rf}}=0$. The spectra calculated for R^3 and CIR^3 are peaked at 5.0 and 3.0 ppm, respectively (not shown). These values agree with the theoretical $\mu\sigma_2$ values given by the σ_2 value of 10 ppm and the μ values [Eq. (28) for R^3 and Eq. (31) for CIR^3]. We also calculated the spectra observed by PPT–GET or CIPT–GET with the XXXXXXXX phase cycling scheme for various duty factors. The duty factor dependence of the $\mu\sigma_2$ values is shown in Fig. 1. The results obtained by the multistep method agree with the theoretical curves calculated using $\sigma_2=10$ ppm and the theoretical scaling factors [Eq. (26) for PPT and Eq. (29) for CIPT]. All these results indicate that the theoretical scaling factors calculated using

TABLE III. Values of $\sigma_2^{\mathrm{calc}}-10$ ppm. σ_2^{calc} is the σ_2 value (in ppm) obtained from a γ-encoded spectrum numerically calculated by the multistep method for R^3, CIR^3, PPT–GET, or CIPT–GET under the presence of rf-amplitude missetting δ_{rf}. The value of 10.0 ppm is that assumed for the calculations.

δ_{rf}	R^3	CIR^3	PPT–GET	CIPT–GET
$+0.1\pi$	4.8 ppm	−1.3 ppm	−0.9 ppm	−0.1 ppm
-0.1π	4.4 ppm	1.8 ppm	−0.9 ppm	0.1 ppm

the zeroth-order average Hamiltonian theory are reliable. Therefore we use these theoretical scaling factors in the following analysis.

We then evaluated the effect of δ_{rf} for R^3, CIR^3, PPT, and CIPT by calculating spectra with rf-field strengths 10% weaker and stronger than the ideal strengths. Table III shows $\sigma_2^{\mathrm{calc}}-10$ (in ppm), which are the differences between the σ_2 values obtained from the calculated spectra (σ_2^{calc}) and the σ_2 values used in the calculation. The results for PPT and CIPT are almost independent of τ_{p} (not shown), and those for $\tau_{\mathrm{p}}=20$ μs are shown in Table III. Both of the σ_2 values obtained for $\delta_{\mathrm{rf}}=\pm 0.1\pi$ in R^3 are considerably larger than 10 ppm. Moreover, the peak intensity is decreased and a large sharp peak at $\sigma_2=0$ ppm appears (not shown). These results can be explained using the zeroth-order average Hamiltonian in Eq. (27): the σ_2 values for $\delta_{\mathrm{rf}}=\pm 0.1\pi$ are calculated to be 14.6 ppm, and the presence of the I_x term causes a sharp peak at 0 ppm. As shown above, the spectrum observed by R^3 is much affected by rf-amplitude missetting and rf-field inhomogeneity. The spectrum obtained by CIR^3 is less sensitive to rf-amplitude missetting than R^3. However, the σ_2 values obtained from the spectra observed by CIR^3 are still substantially different from the expected value (10 ppm). Moreover, a small peak at $\sigma_2=0$ ppm is observed. When PPT–GET is used, this peak shift is reduced to −0.9 ppm and no additional peak except for cycling sidebands[20] is observed. The spectrum obtained by CIPT–GET is much less affected by rf-amplitude missetting than the other three methods and gives a peak at 10 ∓ 0.1 ppm for $\delta_{\mathrm{rf}}=\pm 0.1\pi$. In conclusion, rf-field missetting and rf-field inhomogeneity cause a peak position shift and/or a line shape distortion for R^3, CIR^3, and PPT–GET, and this unfavorable effect can nearly be removed by using CIPT–GET.

IV. RESULTS AND DISCUSSION

In this section, we show that γ-encoded spectra observed by the 2D NMR sequence in which R^3, CIR^3, PPT, or CIPT is applied to ^{13}C in the t_1 period, and no ^{13}C rf field is irradiated in the t_2 period except for an observation 90° pulse. When PPT or CIPT is applied, the FID in the t_1 period is transformed by GET, while FT is applied to the other periods. The 2D spectrum thus obtained represents sharp peaks at $(\omega_1,\omega_2)=(\sigma_{2i},\overline{\sigma_i})$. Figures 2–7 show the results obtained for the ultradrawn polyethylene fiber in order to examine the effects of rf-amplitude missetting, rf-field inhomogeneity, finite pulse width and resonance offset for R^3, CIR^3, PPT, and CIPT. The experiments were performed under MAS with a spinning frequency of 2.00 kHz, unless otherwise indicated. For PPT and CIPT, the phase cycling scheme of $\overline{\mathrm{XXXXXXXX}}$ was used. In Fig. 8, the 2D spectrum of the uniaxially drawn isotactic polypropylene film is given as an example of separate determination of the principal values for a system with more than one chemically inequivalent CSA tensor. We also determined the α_{PR} and β_{PR} distribution from the line shapes of the 2D peaks.

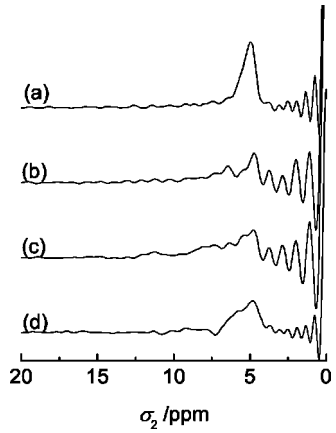

FIG. 2. Experimental γ-encoded spectra observed by R^3 for the ultradrawn polyethylene fiber under MAS with a spinning frequency of 2.00 kHz, the fiber axis being parallel to the spinning axis. The rf-field strength was set to 4.0 kHz (R^3 matching strength) (a), (d), 3.8 kHz (b), and 4.2 kHz (c). While the spectra (a)–(c) were observed with the rf irradiation at $\overline{\sigma}$, the spectrum (d) was observed with the rf irradiation at a frequency 1 kHz lower than $\overline{\sigma}$. The horizontal scale is adjusted according to the theoretical scaling factor of 1/2.

Figure 2 shows the cross sections ($\omega_2=\overline{\sigma}$) of γ-encoded 2D spectra observed using R^3. When a rf-field strength of 4.0 kHz (R^3 matching strength) was used, a sharp peak appeared at $\sigma_2=5.0$ ppm in the spectrum [Fig. 2(a)]. However, the σ_2 value is somewhat larger than the expected value ($7.0\times\sin^2\theta_{\mathrm{m}}=4.7$ ppm) calculated from the previously reported CSA,[7] and a large peak appears at $\sigma_2=0$ ppm. The peak at 0 ppm should considerably be reduced by baseline correction of the FID. When we used rf-field strengths 5% weaker [Fig. 2(b)] and 5% stronger [Fig. 2(c)] than the R^3 matching strength, the line shapes were severely distorted. This is because the spectrum observed by R^3 is significantly affected by δ_{rf} as shown by the zeroth-order average Hamiltonian of Eq. (27). The error term in Eq. (27) may cause no problem for a system with a large σ_2 value as previously shown by numerically calculated spectra of a polycrystalline sample.[21] However, the error term prevents us from determining the σ_2 value precisely when σ_2 is small. The R^3 spectrum is also sensitive to resonance offset: when the rf field was irradiated at a frequency 1 kHz lower than $\overline{\sigma}$, the line shape was distorted as shown in Fig. 2(d). This distortion is partially caused by the mismatch of the R^3 condition: rf irradiation with the offset frequency of 1 kHz produces an effective field 3% larger than the R^3 matching strength. This effect is reduced when higher-speed sample spinning (and hence a larger rf field) is applied.

Note that R^3 with the rf-field strength equal to the spinning frequency[21] and the TC5 sequence[24] recover no CSA in the present case for the following reason. One ^{13}C CSA principal axis in the crystalline component of polyethylene

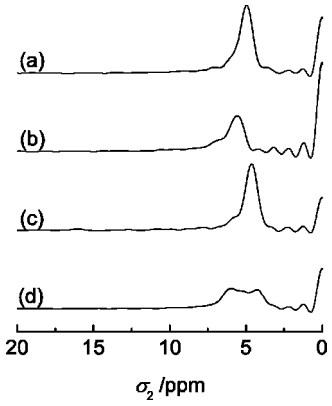

FIG. 3. Experimental γ-encoded spectra observed by CIR[3] for the ultradrawn polyethylene fiber under MAS with a spinning frequency of 2.00 kHz, the fiber axis being parallel to the spinning axis. The rf-field strength was set to 8.0 kHz (CIR[3] matching strength) (a), (d), 7.6 kHz (b), and 8.4 kHz (c). While the spectra (a)–(c) were observed with the rf irradiation at $\overline{\sigma}$: the spectrum (d) was observed with the rf irradiation at a frequency 1 kHz lower than $\overline{\sigma}$. The horizontal scale is adjusted according to the theoretical scaling factor of $2\sqrt{2}/3\pi$.

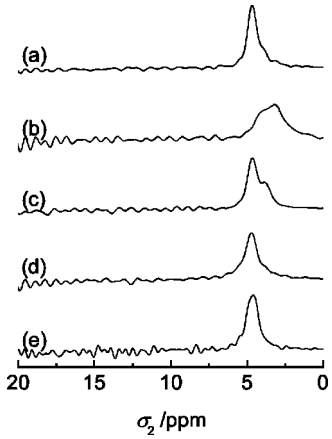

FIG. 4. Experimental GET spectra obtained by PPT–GET for the ultradrawn polyethylene fiber under MAS with a spinning frequency of 2.00 kHz, the fiber axis being parallel to the spinning axis. The $XX\overline{XXXXX}XX$ phase cycling scheme was used. A conventional π pulse width τ_p of 20 μs was used. These spectra were observed with a rf-field strength of 25 kHz $(1/2\tau_p)$ (a), (d), (e), and that of 15% weaker (b) and that of 15% stronger (c) than $1/2\tau_p$. While the spectra (a)–(c) were observed with the rf irradiation at $\overline{\sigma}$: the spectra (d) and (e) were observed with the rf irradiation at the frequencies 2 kHz and 3 kHz lower than $\overline{\sigma}$, respectively. The horizontal scale is adjusted according to the theoretical scaling factor.

should be parallel to the polyethylene chain from the molecular symmetry as indeed observed.[7,25–28] Thus we can assume that z^{PAS} is parallel to the symmetry axis ($\beta_{\mathrm{PR}}=0$), so that σ_1 vanishes. Both R[3] with the rf-field strength equal to the spinning frequency and the TC5 sequence do not restore σ_2, so that no information on CSA is obtained in polyethylene by these sequences.

Figure 3 shows γ-encoded spectra observed using CIR[3]. The spectrum [Fig. 3(a)] observed under a rf-field strength of $4\omega_r/2\pi=8.0$ kHz (CIR[3] matching strength) exhibits a sharp peak at $\sigma_2=4.9$ ppm, which is slightly larger than the expected value of 4.7 ppm, and also a peak at $\sigma_2=0$ ppm with a reduced intensity. For a rf-field strength of 8.4 kHz, the peak was slightly broadened and the peak position was shifted to 5.6 ppm [Fig. 3(b)], while the peak in Fig. 3(c), which was obtained with the strength of 7.6 kHz, was not broadened and represents a peak at 4.6 ppm. No line shape distortion took place contrary to R[3]. These results indicate that the spectrum observed by CIR[3] is less affected by rf-amplitude missetting and rf-field inhomogeneity than the spectra observed by R[3]. However, the CIR[3] spectrum is sensitive to resonance offset; the line shape was distorted when the rf field was irradiated at a frequency 1 kHz lower than $\overline{\sigma}$ [Fig. 3(d)]. The mismatch of the R[3] condition partially causes the line shape distortion in the CIR[3] spectrum as well as the R[3] spectrum.

Figure 4 presents some spectra observed by PPT–GET. The spectrum obtained with a rf-field strength of $1/2\tau_p=25$ kHz has a peak at 4.7 ppm [Fig. 4(a)], which well agrees with the expected value of 4.7 ppm. The peak is somewhat sharper than those for R[3] and CIR[3]. The peak in Fig. 4(b) which was observed with a rf-field strength 15% weaker than $1/2\tau_p$ is shifted to the low-frequency side with a severe line shape distortion as numerically predicted. Figure 4(c) shows the spectrum obtained at a rf-field strength 15% stronger than $1/2\tau_p$. Although the numerical calculation for a rf-field strength 10% stronger than $1/2\tau_p$ results in a low-frequency shift (Table III), the peak position in Fig. 4(c) agrees with that in Fig. 4(a) and the line shape of the peak in Fig. 4(c) is less distorted than that in Fig. 4(b). This asymmetric nature, which was also observed in the CIR[3] experiments, can be explained by the fact that the rf-field strength was calibrated using a sample (5.5 mm in length) much smaller than the polyethylene fibers (20 mm in length), in the sample coil with a length of 14 mm. The peak position remains at 4.7 ppm, even if the rf-field frequency is 2 kHz lower than $\overline{\sigma}$ [Fig. 4(d)]; however, the linewidth slightly increases. Further off-resonance irradiation (3 kHz lower than $\overline{\sigma}$) causes a small shift to 4.6 ppm and a further slight line broadening [Fig. 4(e)].

Spectra observed by CIPT–GET are given in Fig. 5. The σ_2 value determined with a rf-field strength of $1/2\tau_p=25$ kHz is 4.7 ppm [Fig. 5(a)]. It agrees well with the ex-

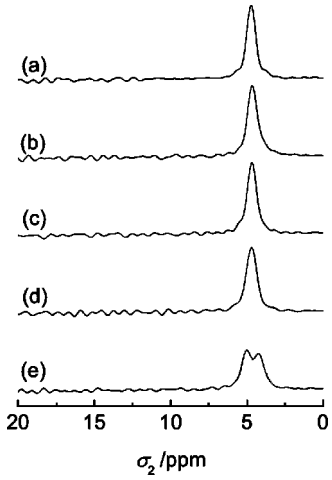

FIG. 5. Same as Fig. 4 except for the use of CIPT–GET. The corresponding composite inversion pulse length is 40 μs ($\tau_p=20$ μs).

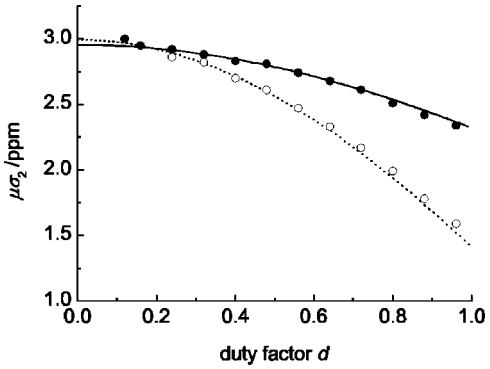

FIG. 6. Experimentally observed and simulated $\mu\sigma_2$ values of the ultradrawn polyethylene fiber under MAS with a spinning frequency of 2.00 kHz, the fiber axis being parallel to the spinning axis. The $\overline{\text{XXXXXXX}}$ phase cycling scheme was used. The rf field was irradiated at $\overline{\sigma}$. The circles represent the experimental values obtained by PPT–GET (●) and CIPT–GET (○). The simulated curves were obtained using the theoretical scaling factor μ [Eq. (26)] with the best-fit parameter of $\sigma_2=4.64$ ppm for PPT–GET (solid line) and using Eq. (29) with $\sigma_2=4.70$ ppm for CIPT–GET (dotted line).

pected value, and moreover no distortion of the line shape was observed. The linewidth [0.62 ppm in Fig. 5(a)] is narrower than those for R^3 [1.05 ppm in Fig. 2(a)], CIR^3 [1.00 ppm in Fig. 3(a)], PPT–GET [0.75 ppm in Fig. 4(a)], and OMAS at $\theta=\pi/2$ (0.83 ppm, spectrum not shown), although it is still broader than that for MAS (0.24 ppm, spectrum not shown). The line shapes and peak positions were unchanged even if rf-field strengths 15% weaker [Fig. 5(b)] and 15% stronger [Fig. 5(c)] than $1/2\tau_p$ were used. As numerically predicted, these experimental results demonstrate that CIPT is very robust for rf-amplitude missetting and rf-field inhomogeneity. When the rf-field was irradiated at a frequency 2 kHz lower than $\overline{\sigma}$, the peak position was still unchanged [Fig. 5(d)]. However, further off-resonance irradiation (3 kHz from $\overline{\sigma}$) caused a severe distortion of the line shape [Fig. 5(e)]. Thus the rf field must be applied within ± 2 kHz from $\overline{\sigma}$.

As shown above, the spectrum obtained by PPT–GET or CIPT–GET is less affected by resonance offset, rf-amplitude missetting, and rf-field inhomogeneity than that by R^3 or CIR^3. However, it should be noted that the signal obtained by R^3 or CIR^3 should be stronger than that by PPT–GET or CIPT–GET, because the former is sinusoidally modulated, while the latter is described by the zeroth-order Bessel function.

Figure 6 shows the duty factor dependence of the $\mu\sigma_2$ values obtained by PPT–GET and CIPT–GET. Using Eq. (26) and Eq. (29), the best-fit curves for PPT–GET and CIPT–GET were obtained for $\sigma_2=4.64$ ppm and 4.70 ppm, respectively, which agree with the expected value (4.7 ppm). The $\mu\sigma_2$ values obtained with the shortest τ_p values for PPT under MAS ($d=0.12$), CIPT under MAS ($d=0.24$), and CIPT under OMAS ($d=0.20$; see Fig. 7) slightly deviate from the individual simulated values. This may be caused by errors in the estimation of the duty factors: for a very short pulse width, it is very difficult to estimate the effective pulse width correctly because of a discrepancy between the actual pulse shape and the ideal rectangular shape. Figure 6 also shows that the $\mu\sigma_2$ values experimentally obtained by either sequence agree well with the $\mu\sigma_2$ values obtained by simulations using the theoretical scaling factor even for large duty factors.

Because of the high compensation for resonance offset, rf-amplitude missetting, and rf-field inhomogeneity, CIPT provides reliable results. However, PPT can be used under higher-speed spinning than CIPT, since the maximum spinning frequency of $1/4\tau_p$ for PPT is twice higher than that of $1/8\tau_p$ for CIPT. One may think that these sequences can be used under high-speed spinning by increasing the ^{13}C rf-field strength. However, the maximum strength of the ^{13}C rf field should be limited to about one-third of the ^1H rf-field strength, in order to avoid $^1H-^{13}C$ recoupling, when the ^1H and ^{13}C rf fields are simultaneously irradiated as previously reported.[29] Therefore, the ^1H rf-field strength must also be increased for attaining high-speed spinning.

We can determine the three principal values of the CSA tensor for the polyethylene carbon, using the σ_2 value (4.70 ± 0.04 ppm) obtained by CIPT–GET together with $\sigma^{iso}=32.70\pm0.04$ ppm and $\overline{\sigma}=43.5\pm0.1$ ppm; the latter was obtained by OMAS at $\theta=\pi/2$. However, it should be noted that there are two possible solutions due to the quadratic equation of Eq. (11). When a principal axis is parallel to the symmetry axis, the two solutions are identical. If not, we can choose the correct solution by determining the σ_2 value at another angle θ: the solution which does not change by changing θ is the true solution. For the present case, it is known that a principal axis is parallel to the symmetry axis.[7,25–28] Therefore using Eqs. (2), (7), and (11), we obtain a unique solution for the methylene carbon in polyethylene: $(\sigma_{xx}^{PAS},\sigma_{yy}^{PAS},\sigma_{zz}^{PAS})=(50.6\pm0.1,36.5\pm0.1,11.1\pm0.3)$ ppm. These values agree well with the previously reported values: $(\sigma_{xx}^{PAS},\sigma_{yy}^{PAS},\sigma_{zz}^{PAS})=(50.1,36.4,12.5)$ ppm from a 1D powder pattern (Ref. 30), (49.5,36.8,11.9) ppm (Ref. 25) (we assumed σ^{iso} to be 32.7 ppm), and $(51.4\pm1.3,38.9\pm1.3,12.9\pm1.3)$ ppm (Ref. 31) from 1D spectra of drawn polyethylene and (50.1,36.7,12.7) ppm by switching-angle sample spinning and separated local field (SLF) spectroscopy (Ref. 27). All the previous results rely on the observation and simulation of a 1D or 2D powder pattern, which inevitably cause the deterioration of accuracy. On the other hand, the present method provides the principal values from the positions of sharp peaks; no simulation is needed, and the accuracy is better than previously reported.

The above experiments were performed under MAS. However, even under OMAS, we can observe sharp peaks at $\overline{\sigma}$ without pulses and at σ_2 with R^3, CIR^3, PPT–GET, or CIPT–GET for uniaxially oriented samples with the symmetry axis parallel to the spinning axis. Thus, 2D correlation spectra peaked at $(\sigma_2,\overline{\sigma})$ can be observed under OMAS as well as MAS. Figure 7 shows the duty factor dependence of the $\mu\sigma_2$ values obtained by CIPT–GET under OMAS at $\theta=\pi/2$. The best-fit curve was obtained for $\sigma_2=7.03$ ppm which agrees with the expected value of 7.0 ppm.

When more than one distinct CSA exists, they cannot simultaneously be represented by the positions of sharp lines by GET in a static sample.[7] However, the present methods under sample spinning provide 2D peaks at $(\sigma_2,\overline{\sigma})$ for all

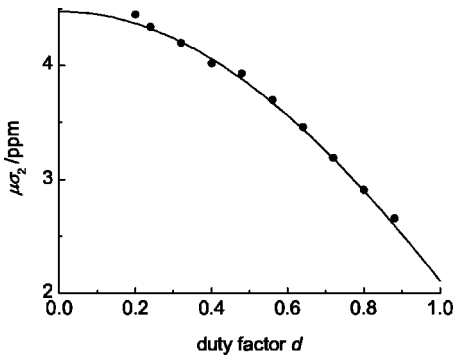

FIG. 7. Experimentally obtained (•) and simulated (solid line) $\mu\sigma_2$ values of the ultradrawn polyethylene fiber under OMAS with a spinning frequency of 2.00 kHz at $\theta=\pi/2$, the fiber axis being parallel to the spinning axis. The rf field was irradiated at $\overline{\sigma}$. The experimental values were obtained by CIPT–GET with the XXXXXXXX phase cycling scheme. The simulated curve was obtained using the theoretical scaling factor μ [Eq. (29)] with the best fit parameter $\sigma_2=7.03$ ppm.

the chemically distinct nuclei. As an example, the 2D spectrum observed for a uniaxially drawn isotactic polypropylene film is shown in Fig. 8. The angle θ was set to $\pi/2$ so that we used the MLEV4 phase cycling scheme with the cycle time shorter than that of the XXXXXXXX phase cycling scheme. A spinning frequency of 2.20 kHz was used. The rf field was irradiated at 34.5 ppm, so that the condition that the rf field should be irradiated within ± 2 kHz from $\overline{\sigma}$ was satisfied for all the three peaks in the OMAS spectrum. The spectrum shows the three 2D peaks with linewidths broader than that in polyethylene. This line broadening shows that the polypropylene chain axes do not perfectly align along the z^{rot} axis. We analyze the chain-orientation distribution below.

First, neglecting the chain-orientation distribution, we roughly estimate the principal values of the CSA tensors from the peak positions. With the help of the MAS spectral assignments,[32] we made the OMAS spectral assignments

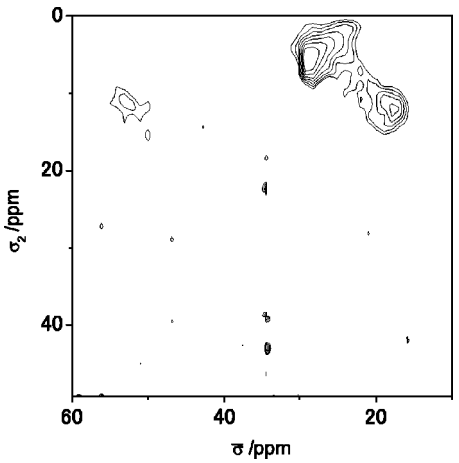

FIG. 8. 2D spectrum observed by CIPT–GET with the MLEV4 phase cycling scheme for the uniaxially drawn isotactic polypropylene film under OMAS conditions at $\theta=\pi/2$, the drawn axis being parallel to the spinning axis. The horizontal scale represents the $\overline{\sigma}$ value, and the vertical scale is adjusted according to the theoretical scaling factor to represent the σ_2 value. A spinning frequency of 2.20 kHz, a rf-field strength of 25 kHz, and $\tau_{\mathrm{p}}=20$ μs were used.

from the peak correlation between the OMAS spectrum and the MAS spectrum, which was obtained by a variable-angle spinning experiment.[33] We obtain the σ^{iso} values from the cross-polarization MAS (CPMAS) spectrum: 21.21 ± 0.05 ppm for the methyl carbon, 26.51 ± 0.03 ppm for the methine carbon, and 44.40 ± 0.03 ppm for the methylene carbon. While two peaks with the integral intensity ratio of 1:2 are observed for each of the methyl and methylene carbons in the CPMAS spectrum due to the two distinct inter-chain environments,[34] we used the weighted average value of the two peak positions as σ^{iso}. We roughly estimated the σ_2 and $\overline{\sigma}$ values from the maxima of the 2D peaks: $(\sigma_2,\overline{\sigma})=(12.0,17.4)$ ppm for the methyl carbon, (5.5,28.8) ppm for the methine carbon, and (10.8,53.3) ppm for the methylene carbon. One principal axis for each carbon can be assumed to be along the chain axis from the local symmetry:

$$\beta_{\mathrm{PR}}^{\mathrm{CH}}=\beta_{\mathrm{PR}}^{\mathrm{CH}_2}=\beta_{\mathrm{PR}}^{\mathrm{CH}_3}=0. \tag{43}$$

Using Eq. (43) and the above values of σ^{iso}, σ_2, and $\overline{\sigma}$, we can obtain the principal values of the CSA tensor: $(\sigma_{xx}^{\mathrm{PAS}},\sigma_{yy}^{\mathrm{PAS}},\sigma_{zz}^{\mathrm{PAS}})=(29.4,5.4,31.8)$ ppm for the methyl carbon, (34.3,23.3,21.9) ppm for the methine carbon, and (64.1,42.5,26.6) ppm for the methylene carbon. Thus, we can determine the principal values from the peak positions without simulations even for a system with multiple chemical sites.

Next, we obtain the tensor-orientation distribution and refine the above-obtained CSA principal values. One can directly obtain the distribution by transforming the spectral intensity via Eq. (39), when the principal values are known. However, the precise principal values are not known, and the distribution obtained by the transformation is not very reliable for the present case as follows. The tensor orientation $P(\alpha_{\mathrm{PR}},\beta_{\mathrm{PR}})$ in the uniaxially drawn polypropylene film should be centered at $\beta_{\mathrm{PR}}=0$; intense signals appear near the singularities (a, b, and c in Scheme 1) for each carbon. The reconstructed $P(\alpha_{\mathrm{PR}},\beta_{\mathrm{PR}})$ is unstable, since the resonance frequency is insensitive to α_{PR} and β_{PR} near the singularities. For these reasons we do not perform a direct transformation but simulate the spectra for obtaining the tensor-orientation distribution and refine the CSA principal values. We assume that the polypropylene sample exhibits the *transverse isotropy*,[2] which means the orientation distribution symmetric around both the chain axis and the z^{rot} axis: the angle α^{chain} representing the chain orientation around the chain axis is homogeneously distributed, and the orientation distribution can be characterized only in terms of the angle β^{chain} between the chain axis and the z^{rot} axis. Since the z^{PAS} axis is parallel to the chain axis, the angle α_{PR} is uniformly distributed, and the orientation function of the chain axis $P(\beta^{\mathrm{chain}})$ can be represented by that of the z^{PAS} axis $P(\beta_{\mathrm{PR}})$ for each carbon:

$$P(\beta^{\mathrm{chain}})=P(\beta_{\mathrm{PR}}^{\mathrm{CH}_3})=P(\beta_{\mathrm{PR}}^{\mathrm{CH}_2})=P(\beta_{\mathrm{PR}}^{\mathrm{CH}}). \tag{44}$$

We assumed a uniaxial Gaussian distribution of the chain axis centered at $\beta^{\mathrm{chain}}=0$ (Ref. 13):

$$P(\beta^{\mathrm{chain}})=\exp\left(-\frac{\sin^2\beta^{\mathrm{chain}}}{2\beta_\sigma^2}\right). \tag{45}$$

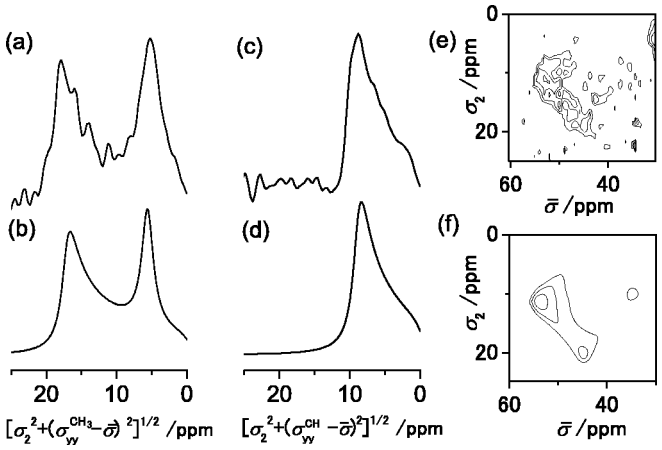

FIG. 9. Experimental (a), (c), (e) and simulated (b), (d), (f) spectra of the uniaxially drawn polypropylene film. The experimental spectra are extracted from Fig. 8. The methyl (a), (b) and methine (c), (d) slices of the 2D $\sigma_2/\bar{\sigma}$ spectra along a line parallel to $\sigma_2=-|\sin^2\theta/2P_2(\cos\theta)|\bar{\sigma}$ and $\sigma_2=|\sin^2\theta/2P_2(\cos\theta)|\bar{\sigma}$ passing the point $(\sigma_2,\bar{\sigma})=(0,\sigma_{yy}^{CH_3})$ and $(0,\sigma_{yy}^{CH})$, respectively, are shown. In spectrum (a) the methine resonance is overlapped at $[\sigma_2^2+(\bar{\sigma}-\sigma_{yy}^{CH_3})^2]^{1/2}=5$ ppm. The 2D spectra (e), (f) represent the methylene resonances. The spectrum (e) is plotted with a different contour level from that used in Fig. 8. The simulated spectra were calculated using the orientational distribution $P(\beta^{chain})=\exp(-\sin^2\beta^{chain}/2\beta_\sigma^2)$ with $\beta_\sigma=40°$ and the chemical shift principal values of $(\sigma_{xx}^{PAS},\sigma_{yy}^{PAS},\sigma_{zz}^{PAS})=(30.3,6.0,30.3)$ ppm for the methyl carbon, (34.9, 22.3, 22.3) ppm for the methine carbon, and (66.3, 43.5, 23.4) ppm for the methylene carbon. Lorentzian broadening with a FWHM of 2 ppm was convoluted along both the $\bar{\sigma}$ axis and the σ_2 axis in the simulated spectra.

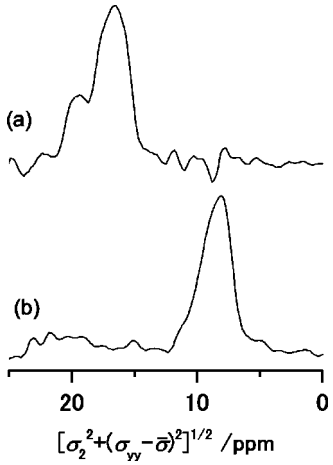

FIG. 10. The 1D slices of the 2D $\sigma_2/\bar{\sigma}$ spectra (Fig. 8) (a) along a line parallel to $\sigma_2=|\sin^2\theta/2P_2(\cos\theta)|\bar{\sigma}$ for the methyl carbon and (b) along $\sigma_2=-|\sin^2\theta/2P_2(\cos\theta)|\bar{\sigma}$ for the methine carbon. The spectra show sharp resonances without the α_{PR}, β_{PR}, and γ_{PR} broadening.

The full width at the half maximum (FWHM) $\Delta\beta$ is given by $\Delta\beta=2(2\ln 2)^{1/2}\beta_\sigma$ (Ref. 13). We symmetrize the CSA tensors of the methyl and methine carbons by averaging the nearest two components: $(\sigma_{xx}^{PAS},\sigma_{yy}^{PAS},\sigma_{zz}^{PAS})=(30.6,5.4,30.6)$ ppm for the methyl carbon and (34.3,22.6,22.6) ppm for the methine carbon. We use these principal values together with the above values for the methylene carbon as a starting point in the simulation analysis, and then refine these values.

Figure 9 shows experimental and simulated spectra of 1D slices of the $\sigma_2/\bar{\sigma}$ powder pattern (Fig. 8) for the methyl and methine carbons and a part of the 2D powder pattern for the methylene carbon. From the simulations we obtain the β_σ value to be $40°\pm6°$ corresponding to $\Delta\beta=94°$ and the principal values $(\sigma_{xx}^{PAS},\sigma_{yy}^{PAS},\sigma_{zz}^{PAS})$ of the CSA tensor to be $(30.3\pm0.5,6.0\pm1.0,30.3\pm0.5)$ ppm for the methyl carbon, $(34.9\pm1.0,22.3\pm0.5,22.3\pm0.5)$ ppm for the methine carbon, and $(66.3\pm0.5,43.5\pm0.5,23.4\pm0.5)$ ppm for the methylene carbon. These values agree well with the previously reported values of $(32\pm0.8,3\pm0.8,32\pm0.8)$ ppm for the methyl carbon, $(38\pm0.8,21\pm0.8,21\pm0.8)$ ppm for the methine carbon, and $(65\pm0.8,44\pm0.8,26\pm0.8)$ ppm for the methylene carbon, which were obtained via the 2D powder patterns observed under OMAS–SLF.[32] The peak positions of the simulated 1D slices for the methyl and methine carbons slightly differ ($\sim$1 ppm) from those in the experimental spectra. This may be caused by a slight nonaxial symmetry of the CSA tensors which we assumed to be axially symmetric. As shown above, we can precisely determine both the principal values of the CSA tensors and chain-orientational distribution by 2D $\sigma_2/\bar{\sigma}$ correlation experiments with 2D spectral simulations, even when the chain orientation is distributed.

While we want to obtain the chain-orientation distribution $P(\beta^{chain})$, it is $P(\beta_{PR})$ that we can directly obtain from the NMR experiments. However, we can easily obtain $P(\beta^{chain})$ using Eq. (44), as for the polypropylene sample with one principal axis parallel to the chain axis. Even if no principal axis is parallel to the chain axis, we can get $P(\beta^{chain})$ by the moment expansion of $P(\beta_{PR})$ as long as the transverse isotropy is satisfied.[13]

Figure 10 shows a 1D slice of the 2D $\sigma_2/\bar{\sigma}$ spectrum for the polypropylene sample (Fig. 8) along a line parallel to $\sigma_2=|\sin^2\theta/2P_2(\cos\theta)|\bar{\sigma}$ for the methyl carbon and $\sigma_2=-|\sin^2\theta/2P_2(\cos\theta)|\bar{\sigma}$ for the methine carbon. The slice direction is perpendicular to the line on which a powder pattern for an axially symmetric CSA tensor appears. These slices should show sharp peaks unaffected by orientational distribution. The residual line broadening is caused by the nonaxial symmetry of these CSA tensors in addition to the linewidth of a spin packet. When the CSA tensor slightly shows asymmetry, the resonances exhibit the linewidth $(P_2(\cos\theta)^2+\sin^4\theta/4)^{1/2}\Delta\sigma$, where $\Delta\sigma$ is the difference between the nearest two principal values. The linewidths in Fig. 10 are 3.0 ppm and 2.6 ppm; considering the Lorentzian broadening (2 ppm) used in the simulations of Fig. 9, we roughly estimate the linewidths due to $\Delta\sigma$ to be 1.0 and 0.6 ppm for the methyl carbon and the methine carbon, respectively. Thus, the $\Delta\sigma$ values are ca. 1.4 ppm for the methyl carbon and ca. 1.0 ppm for the methine carbon. These values are comparable to the experimental error for determination of the principal values, so that we do not need to make a correction for the nonaxial symmetry of the CSA tensors.

V. CONCLUSION

The methods of R^3, CIR^3, PPT–GET, and CIPT–GET which provide γ-encoded spectra are proposed in order to obtain the σ_2 values from the sharp peak positions in uniaxi-

ally oriented samples under MAS or OMAS. In the latter two, the phase cycling schemes of XXXXXXXX should be used, and MLEV4 is recommended for OMAS experiments at $\theta=\pi/2$. In general, a combined use of $\sigma_2/\overline{\sigma}$ and $\sigma_2/\sigma^{\mathrm{iso}}$ 2D NMR enables us to separately determine the principal values of the individual CSA tensors. The spectrum becomes less sensitive to rf-amplitude missetting and rf-field inhomogeneity in order of R^3, CIR^3, PPT–GET, CIPT–GET. The sample spinning frequency can be twice higher in R^3 and PPT than in CIR^3 and CIPT, respectively. The signal sensitivity is considerably higher in R^3 and CIR^3 than in PPT–GET and CIPT–GET. If one applies R^3 or CIR^3, however, it should be noted that careful calibration of the rf-field strength is crucial. When the Euler angles α_{PR} and β_{PR} are distributed, 2D peaks in $\sigma_2/\overline{\sigma}$ spectra under OMAS conditions show two-dimensionally broadened line shapes. The orientational distribution can directly be obtained from the line shapes. The present methods can be used as an alternative to the DECODER experiments,[12,13] which provide the orientation distribution by sample flipping. While the present approach does not provide information on the distribution of γ_{PR} contrary to DECODER, the present method has an advantage in that it can be performed using a conventional CPMAS probe. The methods presented in this paper would be useful for studies of uniaxially oriented samples such as drawn polymers, liquid crystals, and biomembranes.

VI. EXPERIMENTS

Ultradrawn polyethylene fibers made by Toyobo Co. Ltd. and uniaxially drawn isotactic polypropylene films made by Toray Industry Inc. were used without further purification. Prior to sample packing, a bundle of polyethylene fibers were glued together by a cyanoacrylate adhesive, and a polypropylene film was rolled at a right angle direction to the symmetry axis. The sample length is 20 mm for polyethylene and 8 mm for polypropylene. Either sample was put in a 5-mm rotor filled with ethylene glycol to reduce line broadening[35,36] due to bulk magnetic susceptibility by susceptibility matching.[7,37]

The NMR experiments were performed on a Chemagnetics CMX-300 spectrometer with a field of 7.1 T. The sample coil length is 14 mm. The TPPM ^{1}H decoupling scheme[38] was employed during acquisition with a rf-field strength of 79–116 kHz. Here continuous wave decoupling was utilized within the t_1 period with a field strength of 89–116 kHz during the ^{13}C pulse intervals and 114–147 kHz during the ^{13}C pulse irradiations. We set the initial magnetization along the x axis, and the real part of the amplitude-modulated signal in the t_1 dimension was acquired. The 2D experiments for polyethylene took typically less than 6 h and that for polypropylene approximately 7 h.

ACKNOWLEDGMENTS

We would like to thank Professor F. Horii of Kyoto University and K. Hirao of Toray Research Center Inc. for providing us with polymer samples. Y.N. thanks the Japan Society for the Promotion of Science for the research fellowships.

[1] M. Mehring, *Principles of High-Resolution NMR in Solids* (Springer-Verlag, Berlin, 1983).
[2] K. Schmidt-Rohr and H.W. Spiess, *Multidimensional Solid-State NMR and Polymers* (Academic Press, London, 1994).
[3] T.M. de Swiet, M. Tomaselli, and A. Pines, Chem. Phys. Lett. **285**, 59 (1998).
[4] T.M. de Swiet, J. Chem. Phys. **110**, 5231 (1999).
[5] T.M. de Swiet, J. Chem. Phys. **112**, 8567 (2000).
[6] See EPAPS Document No. E-JCPSA6-119-002330 for the proof. A direct link to this document may be found in the online article's HTML reference section. The document may also be reached via the EPAPS homepage (http://www.aip.org/pubservs/epaps.html) or from ftp.aip.org in the directory /epaps/. See the EPAPS homepage for more information.
[7] Y. Nishiyama and T. Terao, Chem. Phys. Lett. **352**, 479 (2002).
[8] T.M. Alam, J. Orban, and G. Drobny, Biochemistry **29**, 9610 (1990).
[9] H. Fritzsche, R. Brandes, A. Rupprecht, Z. Song, T. Weidlich, and D.R. Kearns, Nucleic Acids Res. **20**, 1223 (1992).
[10] A.S. Ulrich and A. Watts, Solid State Nucl. Magn. Reson. **2**, 21 (1993).
[11] T.M. Rothgeb and E. Oldfield, J. Biol. Chem. **256**, 1432 (1981).
[12] K. Schmidt-Rohr, M. Hehn, D. Schaefer, and H.W. Spiess, J. Chem. Phys. **97**, 2247 (1992).
[13] B.F. Chmelka, K. Schmidt-Rohr, and H.W. Spiess, Macromolecules **26**, 2282 (1993).
[14] M.E. Rose, *Elementary Theory of Angular Momentum* (Dover, New York, 1967).
[15] F. Bowman, *Introduction to Bessel Functions* (Dover, New York, 1958).
[16] R. Tycko, G. Dabbagh, and P.A. Mirau, J. Magn. Reson. **85**, 265 (1989).
[17] M.H. Levitt, R. Freeman, and T. Frenkiel, Adv. Magn. Reson. **11**, 47 (1983).
[18] A.A. Maudsley, J. Magn. Reson. **69**, 488 (1986).
[19] T. Gullion, D.B. Baker, and M.S. Conradi, J. Magn. Reson. **89**, 479 (1990).
[20] A.J. Shaka, P.B. Barker, C.J. Bauer, and R. Freeman, J. Magn. Reson. **67**, 396 (1986).
[21] Z. Gan, D.M. Grant, and R.R. Ernst, Chem. Phys. Lett. **254**, 349 (1996).
[22] A. Brinkmann and M.H. Levitt, J. Chem. Phys. **115**, 357 (2001).
[23] R.R. Ernst, G. Bodenhausen, and A. Wokaun, *Principles of Nuclear Magnetic Resonance in One and Two Dimensions* (Clarendon Press, Oxford, 1987).
[24] J.D. Gross, P.R. Costa, and R.G. Griffin, J. Chem. Phys. **108**, 7286 (1998).
[25] S.J. Opella and J.S. Waugh, J. Chem. Phys. **66**, 4919 (1977).
[26] D.L. VanderHart, J. Chem. Phys. **64**, 830 (1976).
[27] T. Nakai, J. Ashida, and T. Terao, J. Chem. Phys. **88**, 6049 (1988).
[28] K. Kuwabara and F. Horii, Macromolecules **32**, 5600 (1999).
[29] Y. Ishii, J. Ashida, and T. Terao, Chem. Phys. Lett. **246**, 439 (1995).
[30] J. Urbina and J.S. Waugh, Proc. Natl. Acad. Sci. U.S.A. **71**, 5062 (1974).
[31] D.L. VanderHart, Macromolecules **12**, 1232 (1979).
[32] T. Nakai, J. Ashida, and T. Terao, Magn. Reson. Chem., **27**, 666 (1989).
[33] R. Teeaar, M. Alla, and E. Lippmaa, Org. Magn. Reson. **19**, 134 (1982).
[34] A. Bunn, M.E.A. Cudby, R.K. Harris, K.J. Packer, and B.J. Say, Polymer **23**, 694 (1982).
[35] U. Schwerk, D. Michel, and M. Pruski, J. Magn. Reson. Ser. A **119**, 157 (1996).
[36] A. Kubo, T.P. Spaniol, and T. Terao, J. Magn. Reson. **133**, 330 (1998).
[37] M.E. Stoll and T.J. Majors, J. Magn. Reson. **46**, 283 (1982).
[38] A.E. Bennett, C.M. Rienstra, M. Auger, K.V. Lakshmi, and R.G. Griffin, J. Chem. Phys. **103**, 6951 (1995).